RSC Advances

PAPER

View Article Online
View Journal | View Issue

Cite this: *RSC Adv.*, 2022, **12**, 25449

Novel ultralong and photoactive $Bi_2Ti_4O_{11}/TiO_2$ heterojunction nanofibers toward efficient textile wastewater treatment

Jermyn Juay,[a] Jia-Cheng E. Yang,[b] Hongwei Bai[a] and Darren Delai Sun *[a]

The elimination of dyes from textile wastewater with a lower carbon footprint is highly contingent on the design of green catalysts. Here, we innovatively developed ultralong one-dimensional $Bi_2Ti_4O_{11}/TiO_2$ heterojunction nanofibers *via* electrospinning so as to photocatalytically degrade dyes efficiently and sustainably through the utilisation of renewable solar irradiation. The heterostructured $Bi_2Ti_4O_{11}/TiO_2$ nanofibers exhibited desirable activity in the visible light region through the slight shift of the absorption edge to a longer wavelength. The $Bi_2Ti_4O_{11}/TiO_2$ nanofibers calcined at 550 °C had a lower optical band gap (3.08 eV) than that of the pure TiO_2 (3.32 eV), as evidenced by their higher photocatalytic degradation kinetics of a model dye (Acid Orange 7) (2.5 times greater than those of pure TiO_2). The enhanced visible light photocatalytic performance arose from the formation of both the $Bi_2Ti_4O_{11}/TiO_2$ heterojunction and the effective separation of photogenerated holes and electrons. The employment of ultralong $Bi_2Ti_4O_{11}/TiO_2$ heterojunction nanofibers for dye removal/decolourisation under visible light is an efficient, cost effective and sustainable solution, which will provide significant insights for practical textile wastewater treatment in view of practical engineering applications.

Received 4th April 2022
Accepted 23rd August 2022

DOI: 10.1039/d2ra02181a

rsc.li/rsc-advances

1. Introduction

Wastewater effluents from textile production are considered as one of the largest contributors to water pollution. These effluents have several unique characteristics, such as (1) heavy colour issues due to the presence of various dyes, (2) high chemical oxygen demand leading to high pollution issues, (3) high salinity and heavy metal concentration *etc.*, which make them not readily biodegradable.[1] There are many combinations of conventional wastewater treatment technologies that employ physical, chemical and biological treatment techniques to treat this textile wastewater.[2] It has been found that approaches such as activated carbon,[3] coagulation/flocculation,[4] and membrane technologies[5] could separate the dye contaminants from the aqueous phase to the solid phase, but without completely eliminating them. Therefore, the disadvantages of current techniques are obvious due to their high cost, low treatment efficiency and associated secondary pollution issues for further disposal. To some extent, the resultant sludges are toxic by-products and large carbon footprints are inevitably involved for their further disposal,[6] thus accentuating the need for developing 'cleaner' alternative approaches.[7] With the growing emphasis on sustainability and advancement in technology, the use of TiO_2 photocatalysts has begun to receive increasing attention.[8–10] The employment of nanostructured TiO_2 with renewable solar energy as the energy input for photocatalytic oxidation (PCO) decontamination offers an efficient and cost-effective method for the treatment of this industrial wastewater.[11]

There are several developed approaches used for the synthesis of TiO_2 photocatalyst such as hydrothermal methods,[12] electrochemical anodization[13] and electrochemical deposition,[14,15] of which the one step electrospinning has shown considerable potential as an innovative and 'green' alternative technology,[16] especially in the field of fabricating one-dimensional (1D) nanostructured materials with large length-to diameter ratio and excellent properties for pollutants adsorption, degradation and removal. In general, 1D TiO_2 nanofibers obtained through electrospinning exhibit significant benefits such as high surface-to-volume ratio, open porous structure and unique material properties allowing it to be easily recycled thus permitting it to be employed in various industries.[16] However, there are two key limitations of TiO_2 which limits its potential. Firstly, the generation of the photo-excited holes and electrons can only be achieved by UV irradiation (λ < 380 nm) which renders the use of solar irradiation inefficient due to wide band gap of TiO_2 (3.2 eV anatase).[10,17] Secondly, the life time of the photo-excited electrons and holes have limited mobility arising from the recombination of electron–hole pair.[17,18]

Therefore, in order to narrow the band gap and improve its photocatalytic performance, materials chemists and

[a]*School of Civil and Environmental Engineering, Nanyang Technological University, Singapore 639798, Singapore. E-mail: ddsun@ntu.edu.sg*
[b]*CAS Key Laboratory of Urban Pollutant Conversion, Institute of Urban Environment, Chinese Academy of Sciences, Xiamen 361021, China*

environmental engineers have widely explored the use of various metal oxides such as Cu,[19–22] Sr,[23] Fe,[24] Cd,[25] Zn,[26,27] *etc.* Recently, bismuth titanates (BTO)-oriented catalysts have drawn a significant amount of emphasis due to their unique optical properties and potential applications,.[17,18,28] These nanostructured bismuth nanomaterials have shown to be valuable photocatalysts that can effectively and efficiently break down various model dye pollutant in water under UV[29–31] and visible light irradiation.[26,32,33] However, the majority of these BTO catalysts are synthesised from solid state reactions involving multiple stages at high reaction temperature and pressure.[17,34] To date, there has been little knowledge on BTO and TiO_2 heterostructures synthesised through electrospinning approaches. Herein, $Bi_2Ti_4O_{11}/TiO_2$ heterostructure nanofibers were unprecedentedly designed and prepared by an effective one-step electrospinning approach to study their PCO decontamination efficiency for treating textile wastewaters. A key benefit to the heterostructured BTO and TiO_2 from the one-step electrospinning lies in the fact that the uniform mixing of BTO and TiO_2 precursor at molecular level will facilitate the close contact between Bi and TiO_2 in the formed materials, which will greatly improve the electrons transfer allowing for better photocatalytic activity.[17,28]

2. Experimental

2.1 Synthesis of $Bi_2Ti_4O_{11}/TiO_2$ heterostructure nanofibers

2.1.1 Materials. Ethanol (CH_3CH_2OH), acetic acid (CH_3COOH), dimethylformamide (DMF, $(CH_3)_2NCH$), polyvinylpyrrolidone (PVP, $M_w = 1\ 300\ 000$) and bismuth(III) nitrate pentahydrate ($Bi(NO_3)\cdot 5H_2O$) were of analytical grade and used directly without further purification. Tetra *n*-butyl orthotitanate ($Ti(OCH_2CH_2CH_2CH_3)_4$) as a precursor of TiO_2 was of reagent grade.

The precursor solution for electrospinning was prepared as follows: firstly, in a volume ratio of 11 : 3 : 1, ethanol, acetic acid and DMF were mixed to achieve a homogenous solution. Subsequently, 3 wt% of bismuth salt was added to the above mixture and stirred until a clear solution was obtained. 20 wt% of PVP was then dissolved before the titanium component was finally added to the mixture with being magnetically mixed for 6 hours to obtain a clear gel solution for electrospinning.

2.1.2 Fabrication of $Bi_2Ti_4O_{11}/TiO_2$ nanofibers. The $Bi_2Ti_4O_{11}/TiO_2$ heterojunction nanofibers were electrospun using an electrospinning set up as shown in Fig. 1. Facilitated using a syringe pump, the precursor solution was injected at a rate of 10 μL min^{-1} through a 10 mL composite stainless-steel nozzle with an internal diameter of 1 mm. The nozzle tip was subjected to an electrical potential of approximately 23 kV (1.3 kV cm^{-1}), and the electrospun fibers were collected on a rotary drum 16 cm away from the tip of the nozzle. The electrospun composite nanofibers were then left to hydrolyse in air for 6 hours before it was calcined at various temperature with a temperature ramp of 1 °C min^{-1}.

2.2 Photocatalytic activities of $Bi_2Ti_4O_{11}/TiO_2$ nanofibers

Here, a typical industrial dye Acid Orange 7 (AO7) was used as a probe pollutant for evaluating the photodegradation efficiency. The photocatalytic oxidation test was conducted in the reactor vessel shown in Fig. 2. A 20 mg L^{-1} of AO7 (model pollutant) was first prepared before adding 0.5 g L^{-1} of $Bi_2Ti_4O_{11}/TiO_2$ heterostructure nanofiber photocatalyst into the solution. This solution was magnetically stirred in the reactor for 120 min to ensure homogeneity of the photocatalyst in the solution and establish an adsorption equilibrium between the pollutant and nanofiber photocatalyst. Thereafter, the irradiation source was turned on and at pre-determined intervals of illumination, 2.0 mL of reaction solution was drawn and the decrease in concentration of the AO7 solution was measured using a spectrophotometer (UV-1800 Shimadzu© UV-vis spectrophotometer).

The designed photoreactor comprises of 2 components, the first being the outer reactor vessel in which the $Bi_2Ti_4O_{11}/TiO_2$ nanofibers as a photocatalyst was suspended. The second component, the inner quartz cooling jacket where a 360 W high pressure sodium lamp (Riko, HNL-360A) with a luminous efficacy of 80–125 lm W^{-1} was used as the UV-vis light source. The cooling jacket was constantly cooled using a peristaltic pump to ensure that optimum operation temperature.[35]

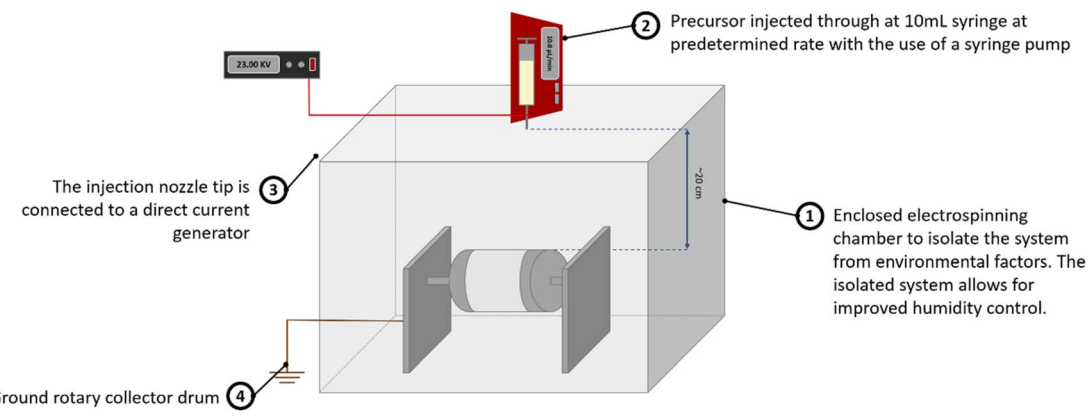

Fig. 1 Schematic diagram of electrospinning chamber.

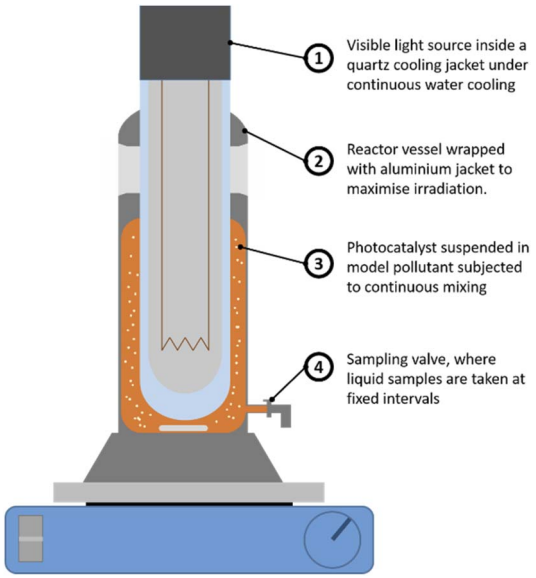

Fig. 2 Schematic diagram of photocatalytic oxidation reactor.

2.3 Characterisation of $Bi_2Ti_4O_{11}/TiO_2$ heterostructure nanofibers

The structural morphology of the $Bi_2Ti_4O_{11}/TiO_2$ heterostructure nanofibers were characterised with a field emission scanning electron microscope (Field Emission Scanning Electron Microscope JSM-7600F). The elemental distribution of the as prepared nanofiber was studied with the use of energy-dispersive X-ray spectroscopy (EDX – Oxford Instrument, X-max, 80 mm^2). The high-resolution transmission electron microscope (TEM) images were acquired using a TEM JOEL-2010HR. The X-ray diffraction patterns were recorded on a Bruker D8 advance X-ray diffractometer (XRD) with monochromated high intensity Cu Kα radiation ($\lambda = 1.5418$ Å). The BET (Brunauer, Emmett and Teller) specific surface area and BJH (Barret–Joyner–Halenda) pore size distribution of the heterostructure nanofiber were assessed at liquid nitrogen temperature (77 K) using Quadrasorb evo™. The samples were degassed in a MasterPrep® Degasser at 160 °C for 8 hours prior to the analysis. The UV-vis diffused reflectance (DR) spectra was recoded on a UV-2600 Shimadzu UV-vis and using $BaSO_4$ as a reference.

3. Results and discussion

3.1 Material characterisation

3.1.1 Crystalline properties. The crystal structure of the heterostructure nanofiber was investigated by XRD characterization (Fig. 3). The diffraction patterns of the nanofiber calcined at various temperatures revealed the successful formation of a heterostructure nanostructure with both $Bi_2Ti_4O_{11}$ and TiO_2 crystalline structures. As observed, the $Bi_2Ti_4O_{11}$ diffraction were not prominent due to the low concentration of bismuth precursor and convolution of the diffraction patterns of TiO_2 anatase phase and $Bi_2Ti_4O_{11}$ phase.[17] Moreover, from the increased peak intensity of the $Bi_2Ti_4O_{11}$ species at higher temperatures, it can be suggested that a higher degree of crystallisation is required to enhance the detection of the $Bi_2Ti_4O_{11}$ species. The TiO_2 crystallinity and crystallite size also increased as the calcination temperature increased. It was observed that the strength of the anatase diffraction peaks had been intensified at higher calcination temperature. The progressive narrowing of the width of the anatase peaks was attributed to the growth of the TiO_2 crystal as the calcination temperature increased.[36] This is further corroborated by the calculation of crystallite sizes using the Scherrer equation of the anatase (101) plane diffraction peak (*cf.* Table 1). In addition, from the nature of the XRD patterns, it shows that the presence of the $Bi_2Ti_4O_{11}$ did not affect the phase transformation of the TiO_2, thus implying that the Bi precursor did not substitute Ti to enter the TiO_2 lattice but was formed through a heterojunction which assimilates the $Bi_2Ti_4O_{11}$ crystal phase and TiO_2 crystal phase.[37]

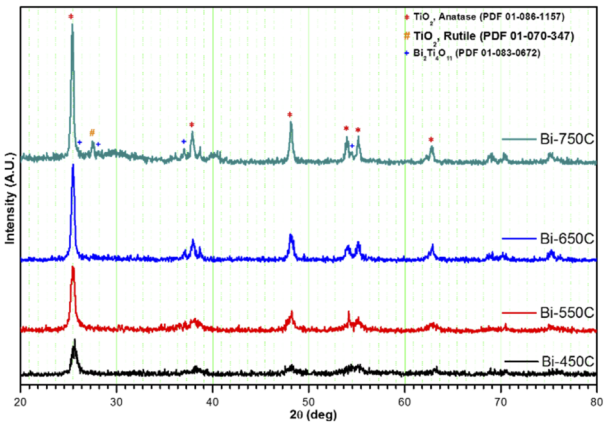

Fig. 3 XRD diffraction patterns of $Bi_2Ti_4O_{11}/TiO_2$ heterostructure nanofibers calcined at various temperatures.

3.1.2 Elemental composition. The XRD analysis as illustrated in Fig. 3 further substantiates the stability of the anatase phase. No phase transformation occurred when the temperatures rising from 450 °C to 750 °C. EDX analysis was conducted to determine the possible elements in the heterostructure nanofibers. As illustrated in the elemental mapping (Fig. 4(a)), the Bi species was highly dispersed within the heterostructure nanofibers, thus implying the homogeneous nature of the electrospinning gel. EDX spectrum as shown in Fig. 4(b) indicates the presence of the 3 elements: Ti, Bi and O. A highly dispersed elemental dispersion helps to optimise the contact between the TiO_2 and $Bi_2Ti_4O_1$ heterojunction, allowing for an efficient electron transfer between the conduction band (CB) phases and resulting in improved photocatalysis.[19]

Moreover, the EDX analysis also revealed that the weight ratio of the bismuth component was 3.34 wt%, which corresponds to the amount of bismuth precursor added to the gel as described in previous Section 2.1.1. This finding supports the fact of weak diffraction peaks for the $Bi_2Ti_4O_{11}$ species as a consequence of the low concentration and well dispersed nature of the Bi precursor.[35]

Table 1 Physiochemical characteristics of synthesised $Bi_2Ti_4O_{11}/TiO_2$ heterostructure nanofiber

Samples	BET specific surface area ($m^2\ g^{-1}$)	Estimated pore diameter (nm) estimated with BJH	Full width at half maximum (deg)	Anatase TiO_2 crystallite size (nm)
Bi-450C	57.56	3.63	0.67	12.64
Bi-550C	34.96	3.64	0.55	15.57
Bi-650C	12.29	3.03	0.38	22.19
Bi-750C	6.39	2.66	0.34	24.94
TiO_2 NF (550C) (anatase phase)	27.582	3.63	0.56	15.18

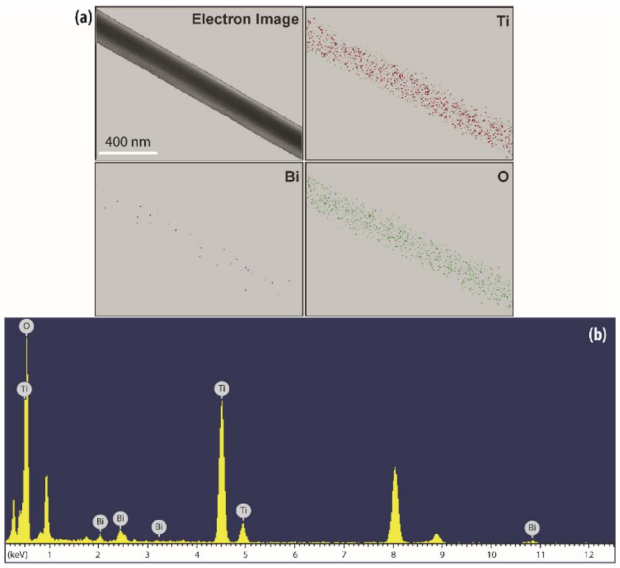

Fig. 4 (a) Elemental mapping for the selected area of Ti, Bi and O elements, (b) EDX spectrum of electron image shown in (a).

3.1.3 Morphology characteristics. The FESEM image in Fig. 5(a) shows the representative morphology of the synthesised heterostructure nanofiber calcined at 550 °C. Evidently, the heterostructure nanofiber have diameters ranging from 70 to 100 nm with an aspect ratio from 25 to 55. The humidity control using N_2 gas prior to the electrospinning ensured the formation of the highly uniform structure. Fig. 5(b) shows the heterostructure nanofiber under higher magnification after calcination at 550 °C. It revealed that the nanofiber possessed a rough and porous surface structure, thus indicating the potential of the heterostructure to provide more active sites for improvement in photocatalytic activity. This change in surface characteristics provides additional sites for adsorption as well as enhances photocatalysis through the provision of more trapping sites, thus extending the life time of charge carriers. The formation of the porous surface structure is a result from the calcination process, which led to the oxidation of organic materials. The polymer binder used in the precursor resulted in the change from a smooth to a porous surface structure as well as the decrease in nanofiber diameter.[23] Most importantly, it allowed the crystallisation of the TiO_2 and $Bi_2Ti_4O_{11}$ phases which is essential in inducing its photocatalytic properties through the phase transformation arising from the thermal treatment.

The TEM image in Fig. 5(c) exemplifies the detailed porous microstructure, which was also observed in Fig. 5(b). The porous structure is conducive for photocatalysis as it provides channels for the reactants to adsorb onto the surface of the nanofibers. In addition, the TEM image shows the nanofiber comprises of granular nanocrystals denoting good crystallinity which is essential to facilitate charge transfer to achieve efficient photocatalytic activity. As presented in Fig. 5(d), the high magnification HRTEM image clearly reveals the distinguished interface contact and continuity between the lattice fringes with interplanar spacing of 0.325 nm and 0.295 nm. These two distinctive lattice fringes correspond to the (101) plane of anatase TiO_2[38] and the (171) plane of $Bi_2Ti_4O_{11}$, respectively,[39] which substantiates the fact that the nanofiber is formed of a heterostructure consisting of anatase TiO_2 and the $Bi_2Ti_4O_{11}$ crystalline phase.

3.1.4 Porous properties and specific surface area. In order to study porosity of the prepared heterostructure nanofibers, BET nitrogen sorption measurements were carried out. When calcination temperature increased from 450 °C to 750 °C, the surface area of samples decreased from 57.56 $m^2\ g^{-1}$ to 6.39 $m^2\ g^{-1}$ (Table 1). Evidently, the decrease in BET specific surface area was consistent with the growth of the anatase TiO_2

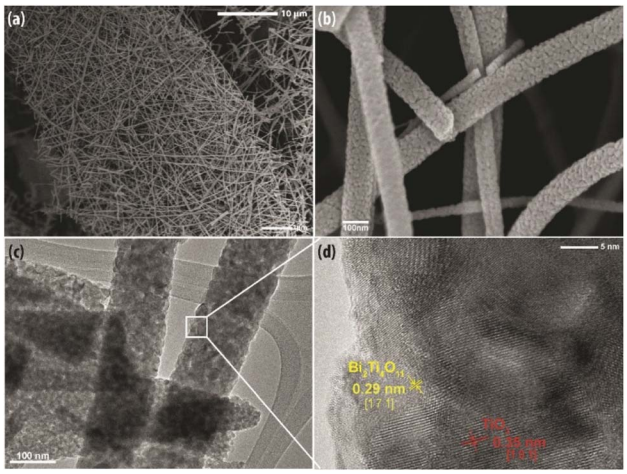

Fig. 5 (a) Low magnification FESEM of $Bi_2Ti_4O_{11}/TiO_2$ (Bi-550C) heterostructure nanofiber after calcination 550 °C. (b) High magnification of FESEM image of Bi-550C. (c) TEM image of Bi-550C. (d) HRTEM image of Bi-550C showing corresponding lattice of TiO_2 and $Bi_2Ti_4O_{11}$.

crystallite at higher temperatures. Moreover, from the N_2 adsorption and desorption isotherms (Fig. 6), the heterostructure nanofiber comprise of mesopores (Table 1).[40] Through the analysis, it was observed that, Bi-450C, Bi-550C, Bi-650C demonstrated a greater adsorbate–adsorbent and adsorbate–adsorbate interactions[41,42] thus implying the occurrence of capillary condensation within mesopores. Meanwhile, the isotherms of Bi-750C showed weak interactions of the adsorbate–adsorbent arising from the enhanced crystal growth at higher calcination temperature.

Additionally, from the BET analysis, it can be noted that the formation of the heterojunction between the $Bi_2Ti_4O_{11}$ and TiO_2 phases enlarged the surface area of the nanofibers. The heterostructure nanofiber showed a 25% increase in the surface area as compared to the pure TiO_2 nanofiber. This increase in BET specific surface area was due to the presence of the well dispersed bismuth elements in the electrospinning precursor, which allowed for the formation of additional active sites comprising of the $Bi_2Ti_4O_{11}$ crystal phase after thermal treatment. This confirms that the formation of the heterostructure structure through the heterojunction has increased the amounts of available reactions sites for the access of reactants for photocatalysis. Furthermore, the observed increase in BET specific surface area also promotes the adsorption and mass transfer of the pollutants. Hence, considering these advantages it is plausible that the heterojunction formed in the $Bi_2Ti_4O_{11}$/TiO_2 heterostructure nanofiber would improve the photocatalytic performance as compared to pure TiO_2 nanofibers.

3.2 Performance evaluation

3.2.1 Degradation of AO7. The photocatalytic activity of the $Bi_2Ti_4O_{11}$/TiO_2 heterostructure nanofiber was evaluated based on the degradation of a model dye, AO7, under visible-light irradiation. There are more than 100 000 kinds of dyes in the industry and AO7 is a water-soluble dye which is considered as a pervasive pollutant due to its potential to form co-contaminants for nitrates. To model the photocatalytic degradation, Langmuir–Hinshelwood kinetics was applied.[43] As shown in eqn (1), the reaction rate (r) can be described as function of the degree of substrate coverage (θ):

$$r = k_i\theta = k_i\left(\frac{KC}{1+KC}\right) \quad (1)$$

where C is the concentration of AO7, k_i is the intrinsic reaction rate constant, and K is the Langmuir adsorption equilibrium constant. As the concentration of AO7 was low, it can be readily presumed that KC was $\ll 1$. Hence, the reaction kinetics can be further simplified as indicated in eqn (2):

$$r = -\frac{dC}{dt} = kKC = kC \quad (2)$$

where k refers to the corresponding reaction rate kinetic constant. Assuming that the decolourisation of AO7 follows a reaction pathway of a pseudo first-order reaction rate, the reaction kinetics can be further simplified in eqn (3).

$$-\ln\frac{C_t}{C_0} = kt \quad (3)$$

where C_t (mg L^{-1}) is the concentration of AO7 at the reaction time of t (min), C_o is the initial AO7 concentration measured after 120 min of dark adsorption and t is the reaction time. Using the pseudo first-order kinetics described in eqn (3), the degradation trend of AO7 is presented in Fig. 6. The logarithms of normalised AO7 concentration were plotted against the irradiation time. The corresponding k constants (gradient) (Table 2) provide a good measure of the overall photodegradation rate since it is apparent from the plot that the degradation trend follows the derived first order kinetics.[44]

3.2.2 Efficiency comparison. The photocatalytic degradation tests (Fig. 7) showed that the $Bi_2Ti_4O_{11}$/TiO_2 heterostructure nanofiber calcined at 550 °C (Bi-550C) had the highest photocatalytic efficiency in the degradation of AO7 under visible light irradiation. The degradation rate of the Bi-550C heterostructure nanofiber was approximately 2 times more efficient than heterostructure nanofiber calcined at 750 °C (Bi-750C, 1.71 × 10^{-2} min^{-1}), suggesting that the physiochemical changes arising from the increase in calcination temperature had a significant impact on the visible light driven photocatalysis.[36]

The heterostructure nanofiber calcined at 750 °C (Bi-750C) has a BET specific surface area of 6.39 m^2 g^{-1}, much lower than that of the nanofiber calcined at 550 °C (Bi-550C, 34.96 m^2 g^{-1}). This indicates that the increase in calcination temperature might have led to the collapse of the microporous structure (which exists at lower temperatures),[45,46] thus resulting in an inferior mass transport between the model pollutant and the heterostructure nanofiber. The less porousness makes more difficult for the pollutant to enter the pore channel of the heterostructure nanofiber.[42,47] Consequently, this resulted in a lower photocatalytic efficiency due to the decrease in the active sites available for reactions (arising from the smaller BET specific surface area).

3.2.3 Simulation of degradation kinetics. Comparing the photocatalytic efficiencies (Table 2) of the Bi-450C, Bi-550C and Bi-650C, the Bi-550C had a photocatalytic efficiency of 1.21 times greater than the Bi-450C and 1.12 times of the Bi-650C,

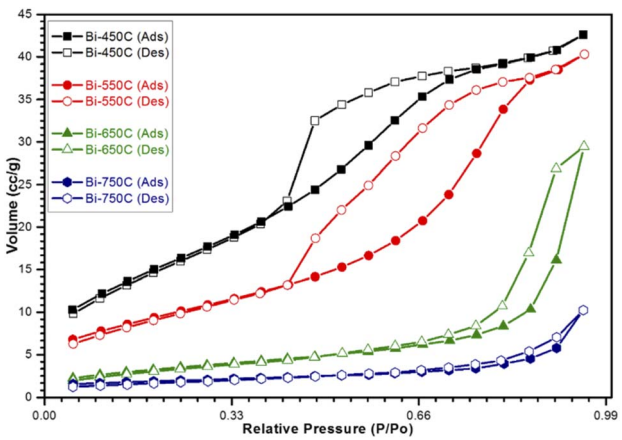

Fig. 6 Nitrogen adsorption/desorption isotherms for calcined $Bi_2Ti_4O_{11}$/TiO_2 heterostructure nanofibers.

Table 2 Modelled degradation kinetics of $Bi_2Ti_4O_{11}/TiO_2$ nanofiber in the degradation of Acid Orange 7

Sample ID	Degradation rate, k (min^{-1})	Standard deviation	R^2	Estimate band gap, E_g (eV)
Photolysis	1.04×10^{-2}	$\pm 7.58 \times 10^{-5}$	0.9639	—
Bi-450C	2.80×10^{-2}	$\pm 2.17 \times 10^{-3}$	0.9594	3.08
Bi-550C	3.38×10^{-2}	$\pm 2.44 \times 10^{-3}$	0.9645	3.08
Bi-650C	3.01×10^{-2}	$\pm 2.48 \times 10^{-3}$	0.9543	3.12
Bi-750C	1.71×10^{-2}	$\pm 1.28 \times 10^{-3}$	0.9622	3.11
TiO_2 NF − 550C	1.28×10^{-2}	$\pm 1.06 \times 10^{-3}$	0.9538	3.32

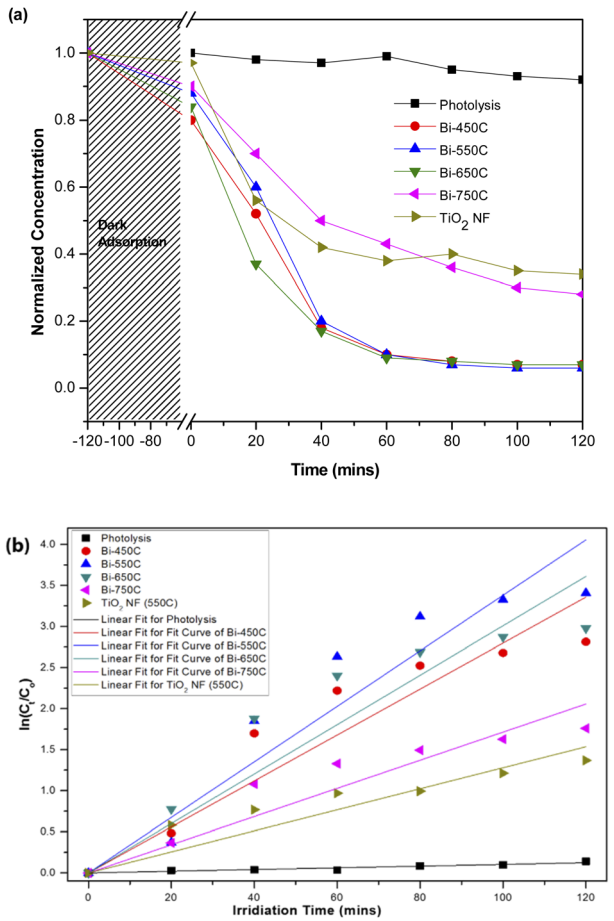

Fig. 7 (a) Normalised concentration curves showing the time-dependent degradation of AO7 by various photocatalysts under visible light irradiation. (b) The modelled pseudo-first order degradation kinetics for various photocatalysts.

respectively. This indicates that the higher crystallinity of both $Bi_2Ti_4O_{11}$ and anatase TiO_2 phase of the heterostructure nanofiber calcined at 550 °C allowed for better charge transport and effective suppression of electrons and hole.[36,42] Despite having a lower surface area than Bi-450C, the Bi-550C has also provided the balance between the bismuth titanate phase and titanium dioxide phases as well as the mesoporous characteristics of the heterostructure nanofiber, favouring photocatalysis.

The $Bi_2Ti_4O_{11}/TiO_2$ heterostructure nanofibers showed a greater photocatalytic efficiency in degrading AO7 under visible light irradiation. As reflected in Table 2, the photo degradation rate of AO7 by Bi-550C was 2.64 times greater than that of pure TiO_2 nanofiber. This is possibly attributed to the enhanced visible light absorption arising from the heterojunction formed between the $Bi_2Ti_4O_{11}$ and the TiO_2 anatase phase (*cf.* Fig. 5(d)). The formation of this heterojunction coupled with the optimised geometry from the microporous structure of the nanofiber allowed for the travel of electron–hole pairs to a shorter diffused pathway to reach the active surface sites of the photocatalyst, therefore ensuring a more effective suppression of the electron–hole recombination.[33,48] Moreover, the diffuse reflectance analysis revealed that the heterostructure nanofibers possessed a lower estimated optical band gap (ranging from 3.08 to 3.11 eV) than that of the pure TiO_2 nanofiber (3.32 eV) (Table 2). The lower band gap (due to the presence of the $Bi_2Ti_4O_{11}$) can be interpreted as an improved light absorption capacity in the visible-light region.[49]

3.3 Photocatalytic stability for practical application

Using Bi-550C as a representative catalyst, we investigated the photocatalytic stability of the $Bi_2Ti_4O_{11}/TiO_2$ heterostructure nanofiber under visible light irradiation. The selected samples were repeatedly used after separation *via* vacuum filtration, and the results are presented in Fig. 8. As shown, there were no significant changes in the photocatalytic activity of Bi-550C after five cycles as the degradation efficiencies of AO7 remained virtually unchanged. This indicates that Bi-550C has good structural stability under visible light irradiation for the photocatalytic decomposition of organic pollutants. Therefore, it is viable to employ these photocatalysts for practical applications as the $Bi_2Ti_4O_{11}/TiO_2$ heterostructure nanofibers have long lifespan for reuse.

3.4 Mechanism revelation

3.4.1 Unique features of $Bi_2Ti_4O_{11}/TiO_2$ heterostructure nanofibers. The efficient photocatalytic performance of the $Bi_2Ti_4O_{11}/TiO_2$ heterostructure nanofibers can be attributed to the combination of the following factors: (i) the enhanced mesoporosity and surface area as discussed can engender more reaction sites for reactant adsorption and mass transfer. (ii) The structural properties of the long nanofibers as well as the anatase TiO_2 phase allow for efficient inhibition of the recombination of photogenerated electrons. To explain the probable electron transfer process between the phases in the $Bi_2Ti_4O_{11}/TiO_2$ heterostructure nanofibers, a schematic diagram shown in

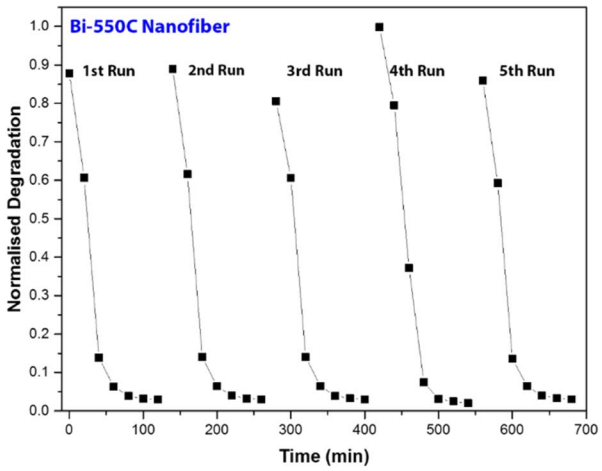

Fig. 8 Photocatalytic stability of heterostructure nanofiber calcined at 550 °C.

Fig. 9 is accordingly proposed based on the AO7 degradation kinetics and crystal structure revealed in the previous sections.

3.4.2 Synergistic effect in photocatalytic enhancement. The transfer of electrons from the excited valence band of the $Bi_2Ti_4O_{11}$ under visible light was promoted due to the up shift of the valence band. Consequently, the photogenerated electrons on the conduction band of the anatase phase is easily utilised for the photocatalytic degradation of AO7 under visible light irradiation. It is proposed that the $Bi_2Ti_4O_{11}$ phase (3.08 eV) lies above that of the anatase TiO_2 (3.32 eV). Moreover, the formation of the heterojunction between the $Bi_2Ti_4O_{11}$ phase and the anatase TiO_2 phase allowed for a favourable separation of electrons and holes due to the effect of the inner electric field.

As shown in Fig. 9, upon harvesting the of photon energy from the simulated solar irradiation, it leads to the excitation of electrons which travels from the valence band (VB) to the conduction band (CB) leaving holes in the VB of the $Bi_2Ti_4O_{11}$ phase. Here due to the heterojunction formed between the phases, the electrons from the CB of the $Bi_2Ti_4O_{11}$ could transfer to the CB of the anatase TiO_2.[17,28] As these photoexcited electrons and holes separate and migrate to the surface of the photocatalyst, it reacts with the aqueous phase generating

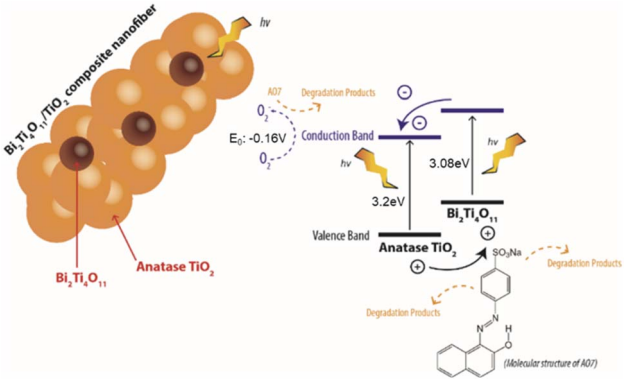

Fig. 9 Schematic diagram of the photo generated electrons and holes in the $Bi_2Ti_4O_{11}/TiO_2$ heterostructure nanofibers.

reducing and oxidising agents degrade AO7. The holes would react with adsorbed hydroxyl groups in the aqueous phase or on the surface of the photocatalyst forming oxidation species such as ($OH^{\bullet}$).[17] Meanwhile, the electrons would react with adsorbed O_2 to produce O_2^- and further degrade AO7. Consequently, through this effective transfer of electrons it would reduce the recombination of the electrons and hole due to the formation of the heterojunction formed between the $Bi_2Ti_4O_{11}/TiO_2$. Therefore, the enhanced photocatalytic activity under visible light irradiation for the $Bi_2Ti_4O_{11}/TiO_2$ can be ascribed to: (1) the enhanced visible light absorption, (2) the good adsorption of model pollutants and (3) the efficient separation of photogenerated charge carriers.[50]

4. Conclusions

This study demonstrated a successful and facile method to synthesize an enhanced visible light driven nanofiber photocatalysts with a heterojunction formed between the $Bi_2Ti_4O_{11}$ (171 phase) and anatase TiO_2 (101 phase). Experimental results revealed that the $Bi_2Ti_4O_{11}/TiO_2$ heterostructure nanofiber showed superior photocatalytic performance than compared to pure TiO_2 in the degradation of the model textile dye AO7 under visible light irradiation. First, the Bi phase was evenly distributed through the heterostructure nanofiber, indicating that the uniform mixing occurring at the molecular level allowed for the formation of heterojunction between the highly crystalline $Bi_2Ti_4O_{11}$ phase and the anatase TiO_2 phase. Second, owing to the formation of this heterojunction, it shifted the absorption edge to a longer wavelength. Third, the presence of the $Bi_2Ti_4O_{11}$ titanate phase coupled with the morphological characteristics of the nanofibers allowed for a more effective transfer of electrons through the reduced recombination of electrons and holes. Fourth, the heterostructure nanofibers have demonstrated excellent photo-stability after undergoing multiple reuses, signifying the robust nature of the heterostructure photocatalyst for practical engineering applications with the use of sustainable visible light or solar utilisation. In view for practical engineering application in treating wastewater through fully exploiting the abundant solar light in sustainable manner, it is believed that the developed $Bi_2Ti_4O_{11}/TiO_2$ heterojunction nanofibers may not only be limited for the employment of textile wastewater degradation but also can be used for other photocatalytic application in environmental remediation.

Conflicts of interest

There are no conflicts to declare.

Acknowledgements

We acknowledge Interdisciplinary Graduate School (IGS) and Nanyang Environment Water Research Institute (NEWRI) for their financial support. We also thank Mr Lua Shun Kuang from IGS for his help and valuable suggestions. The scholarship provided by IGS and NEWRI is appreciated.

Notes and references

1 B. Neppolian, H. C. Choi, S. Sakthivel, B. Arabindoo and V. Murugesan, *Chemosphere*, 2002, **46**, 1173–1181.
2 K. Malachova, Z. Rybkova, H. Sezimova, J. Cerven and C. Novotny, *Water Res.*, 2013, **47**, 7143–7148.
3 C. Zaharia and D. Suteu, *Environ. Sci. Pollut. Res.*, 2013, **20**, 2226–2235.
4 V. Golob, A. Vinder and M. Simonič, *Dyes Pigm.*, 2005, **67**, 93–97.
5 J. Wu, M. A. Eiteman and S. E. Law, *J. Environ. Eng.*, 1998, **124**, 272–277.
6 J. Liu, J. Zheng, G. Yue, H. Li, Z. Liu, Y. Zhao, N. Wang, C. Sun and Z. Cui, *RSC Adv.*, 2022, **12**, 10258–10266.
7 T. Robinson, G. McMullan, R. Marchant and P. Nigam, *Bioresour. Technol.*, 2001, **77**, 247–255.
8 S.-Y. Lee and S.-J. Park, *J. Ind. Eng. Chem.*, 2013, **19**, 1761–1769.
9 M. A. Lazar, S. Varghese and S. S. Nair, *Catalysts*, 2012, **2**, 572–601.
10 A. Fujishima and K. Honda, *Nature*, 1972, **238**, 37–38.
11 V. K. Gupta, R. Jain, A. Mittal, T. A. Saleh, A. Nayak, S. Agarwal and S. Sikarwar, *Mater. Sci. Eng., Proc. Conf.*, 2012, **32**, 12–17.
12 H. Kominami, J. Kato, Y. Takada, Y. Doushi, B. Ohtani, S. Nishimoto, M. Inoue, T. Inui and Y. Kera, *Catal. Lett.*, 1997, **46**, 235–240.
13 J. Ng, X. Zhang, T. Zhang, J.-H. Pan, J.-H. A. Du and D. D. Sun, *J. Chem. Technol. Biotechnol.*, 2010, **85**, 1061–1066.
14 C. Natarajan and G. Nogami, *J. Electrochem. Soc.*, 1996, **143**, 1547–1550.
15 X. Zan and H. Bai, *J. Electrochem. Soc.*, 2021, **168**, 027504.
16 S. Ramakrishna, K. Fujihara, W.-E. Teo, T. Yong, Z. Ma and R. Ramaseshan, *Mater. Today*, 2006, **9**, 40–50.
17 S. S. Lee, H. Bai, S. C. Chua, K. W. Lee and D. D. Sun, *J. Clean. Product.*, 2021, **298**, 126671.
18 H. Bai, Z. Liu and D. D. Sun, *J. Mater. Chem.*, 2012, **22**, 18801–18807.
19 S. S. Lee, H. Bai, Z. Liu and D. D. Sun, *Water Res.*, 2013, **47**, 4059–4073.
20 Y.-C. Pu, W.-H. Lin and Y.-J. Hsu, *Appl. Catal., B*, 2015, **163**, 343–351.
21 Y.-H. Chiu and Y.-J. Hsu, *Nano Energy*, 2017, **31**, 286–295.
22 M.-Y. Kuo, C.-F. Hsiao, Y.-H. Chiu, T.-H. Lai, M.-J. Fang, J.-Y. Wu, J.-W. Chen, C.-L. Wu, K.-H. Wei, H.-C. Lin and Y.-J. Hsu, *Appl. Catal., B*, 2019, **242**, 499–506.
23 H. Bai, J. Juay, Z. Liu, X. Song, S. S. Lee and D. D. Sun, *Appl. Catal., B*, 2012, **125**, 367–374.
24 M. Periyasamy, S. Sain, U. Sengupta, M. Mandal, S. Mukhopadhyay and A. Kar, *Mater. Adv.*, 2021, **2**, 4843–4858.
25 A. T. Nguyen, W.-H. Lin, Y.-H. Lu, Y.-D. Chiou and Y.-J. Hsu, *Appl. Catal., A*, 2014, **476**, 140–147.
26 Y.-C. Chen, T.-C. Liu and Y.-J. Hsu, *ACS Appl. Mater. Interfaces*, 2015, **7**, 1616–1623.
27 W.-H. Lin, Y.-H. Chiu, P.-W. Shao and Y.-J. Hsu, *ACS Appl. Mater. Interfaces*, 2016, **8**, 32754–32763.
28 H. Bai, Z. Liu and D. D. Sun, *J. Am. Ceram. Soc.*, 2013, **96**, 942–949.
29 C. Wang, C. Shao, L. Wang, L. Zhang, X. Li and Y. Liu, *J. Colloid Interface Sci.*, 2009, **333**, 242–248.
30 Y.-H. Chiu, T.-F. M. Chang, C.-Y. Chen, M. Sone and Y.-J. Hsu, *Catalysts*, 2019, **9**, 430.
31 Y.-A. Chen, Y.-T. Wang, H. S. Moon, K. Yong and Y.-J. Hsu, *RSC Adv.*, 2021, **11**, 12288–12305.
32 H. Bai, Z. Liu and D. D. Sun, *ChemPlusChem*, 2012, **77**, 941–948.
33 H. Bai, Z. Liu and D. D. Sun, *Chem. Commun.*, 2010, **46**, 6542–6544.
34 J. Hou, Z. Wang, S. Jiao and H. Zhu, *J. Hazard. Mater.*, 2011, **192**, 1772–1779.
35 S. Xu, J. Ng, A. J. Du, J. Liu and D. D. Sun, *Int. J. Hydrogen Energy*, 2011, **36**, 6538–6545.
36 H. Bai, Z. Liu, L. Liu and D. D. Sun, *Chem. – Eur. J.*, 2013, **19**, 3061–3070.
37 L. Duan, H. Zhu, M. Li, X. Zhao, Y. Wang, Y. Zhang and L. Yu, *J. Alloys Compd.*, 2021, **889**, 161694.
38 J. Ng, S. Xu, X. Zhang, H. Y. Yang and D. D. Sun, *Adv. Funct. Mater.*, 2010, **20**, 4287–4294.
39 H. Shi, H. Tan, W.-b. Zhu, Z. Sun, Y. Ma and E. Wang, *J. Mater. Chem. A*, 2015, **3**, 6586–6591.
40 K. S. W. Sing, *J. Porous Mater.*, 1995, **2**, 5–8.
41 P. Yang, D. Zhao, D. I. Margolese, B. F. Chmelka and G. D. Stucky, *Nature*, 1998, **396**, 152–155.
42 J. H. Pan, H. Dou, Z. Xiong, C. Xu, J. Ma and X. S. Zhao, *J. Mater. Chem.*, 2010, **20**, 4512–4528.
43 X. Wang and T.-T. Lim, *Appl. Catal., B*, 2010, **100**, 355–364.
44 J. Ng, J. H. Pan and D. D. Sun, *J. Mater. Chem.*, 2011, **21**, 11844–11853.
45 S. Madhugiri, B. Sun, P. G. Smirniotis, J. P. Ferraris and K. J. Balkus, *Microporous Mesoporous Mater.*, 2004, **69**, 77–83.
46 Y.-F. Lin and Y.-J. Hsu, *Appl. Catal., B*, 2013, **130–131**, 93–98.
47 P.-Y. Hsieh, Y.-H. Chiu, T.-H. Lai, M.-J. Fang, Y.-T. Wang and Y.-J. Hsu, *ACS Appl. Mater. Interfaces*, 2019, **11**, 3006–3015.
48 T. Cao, Y. Li, C. Wang, C. Shao and Y. Liu, *Langmuir*, 2011, **27**, 2946–2952.
49 J. Zhou, Z. Zou, A. K. Ray and X. S. Zhao, *Ind. Eng. Chem. Res.*, 2007, **46**, 745–749.
50 Q. Guo, C. Zhou, Z. Ma and X. Yang, *Adv. Mater.*, 2019, **31**, 1901997.